

# Synthesis of Rod-Like $\text{Sb}_2\text{Se}_3$ @MWCNT as Conductive-Additive Free Anode for Sodium-Ion Batteries

Taejung Jung<sup>+</sup>,<sup>[a]</sup> Youngho Jin<sup>+</sup>,<sup>[a]</sup> Joon Ha Moon,<sup>[a]</sup> Honggyu Seong,<sup>[a]</sup> Geongil Kim,<sup>[a]</sup> Hyerin Yoo,<sup>[a]</sup> Seunghui Lee,<sup>[a]</sup> Seung-Ryong Kwon,<sup>[a]</sup> Sung Kuk Kim,<sup>\*[a]</sup> and Jaewon Choi<sup>\*[a]</sup>

Antimony selenide ( $\text{Sb}_2\text{Se}_3$ ) is a promising electrode material for sodium-ion batteries (SIBs) due to its high theoretical capacity. However, volume expansion during sodiation/desodiation and the low conductivity of  $\text{Sb}_2\text{Se}_3$  reduce the electrochemical performance. Herein, we synthesized  $\text{Sb}_2\text{Se}_3$  nanorods (NRs) and combined them with multi-walled carbon nanotubes (MWCNTs) using one-step composite process to address these issues. MWCNTs can accommodate volume expansion and provide high conductivity. The fabricated  $\text{Sb}_2\text{Se}_3$  NRs@MWCNT electrode exhibits improved cycle performance and cyclic stability with-

out additional conductive carbons. The  $\text{Sb}_2\text{Se}_3$  NRs@MWCNT electrode showed an enhanced specific capacity of  $440 \text{ mAhg}^{-1}$  at a current density of  $0.1 \text{ Ag}^{-1}$ , compared to  $220 \text{ mAhg}^{-1}$  for the  $\text{Sb}_2\text{Se}_3$  NRs electrode. Additionally, it exhibited good stability at high current density. The in-situ electrochemical impedance spectroscopy (EIS) and Galvanostatic intermittent titration technique (GITT) were used to estimate the electrochemical properties and kinetics of  $\text{Sb}_2\text{Se}_3$  NRs@MWCNT. These results showed that  $\text{Sb}_2\text{Se}_3$  NRs@MWCNT have the potential as a conductive-free anode material in SIBs.

## Introduction

As the demand for electronic devices like portable electronics and electric vehicles increases, the demand for lithium-ion batteries (LIBs) installed in energy storage equipment are under the spotlight as well.<sup>[1,2]</sup> Recently, due to the limitations of LIBs such as the fundamental shortage of lithium resources and high cost, sodium-ion batteries (SIBs) and potassium-ion batteries (PIBs), which have similar energy storage mechanism to LIBs, have attracted attention as alternative energy storage.<sup>[3–6]</sup> However, the large ion radius of  $\text{Na}^+$  (1.02 Å) and  $\text{K}^+$  (1.38 Å) compared to  $\text{Li}^+$  (0.76 Å) lead to sluggish transport and hinders large-scale applications.<sup>[7–11]</sup> The larger ion radius and strong cointercalation in electrolyte of  $\text{K}^+$  result in structural instability and poor electrochemical performance.<sup>[12–14]</sup> S. Chong et al. synthesized  $\text{Sb}_2\text{Se}_3$ @rGO to construct a  $\text{sp}^2$  N-doped carbon coated hierarchical architecture ( $\text{Sb}_2\text{Se}_3$ @rGO@NC) by in situ solvothermal method.  $\text{Sb}_2\text{Se}_3$ @rGO@NC exhibited a capacity of 426.9 and  $261 \text{ mAhg}^{-1}$  at  $0.05 \text{ Ag}^{-1}$  for SIBs and PIBs, respectively.<sup>[15]</sup> Furthermore,  $\text{Na}^+$  is difficult to insert into the interlayers of graphite due to its large ion size. Graphite, which is commercially used as an anode material in LIBs exhibits a low theoretical capacity of  $35 \text{ mAhg}^{-1}$  in SIBs.<sup>[16–19]</sup> Therefore, graphite is not appropriate to be used as electrode material for SIBs, and it calls for the development of anode materials for SIBs is extremely needed.

Conversion, alloying and conversion-alloying type anode materials have gained attraction as anode materials due to their high theoretical capacity and abundant resources. Metal selenide, one of conversion type anode materials, has high specific capacity due to multielectron transfer and good redox reversibility.<sup>[20–22]</sup> Sb-based alloying type anode materials have higher specific capacity and lower working voltage compared to conversion type anode materials.<sup>[14]</sup>  $\text{Sb}_2\text{Se}_3$  has a high theoretical capacity of  $660 \text{ mAhg}^{-1}$ , which is achieved through a conversion and alloying reaction during the sodiation process.<sup>[23]</sup> However, the large volume change and sluggish kinetics of conversion and alloying type anode materials during the sodiation and desodiation processes lead to rapid capacity fading and degrading electrochemical stability.<sup>[24–27]</sup> Structuring nano-size materials<sup>[21,28]</sup> and composites with carbonaceous materials, such as carbon nanotube (CNT) and reduced graphene oxide (rGO), are widely employed to tackle these issues.

Multi-walled carbon nanotubes (MWCNTs) with a 1D tubular structure show significant synergy when combined with active materials for electrode due to high conductivity and large specific surface area.<sup>[29,30]</sup> A large specific surface area can improve ion transfer by increasing the contact between the electrode and the electrolyte. High conductivity can enhance the electrical properties of the active materials.<sup>[31,32]</sup> Furthermore, MWCNTs can mitigate the aggregation of active materials, increasing structural stability and the number of active sites.<sup>[33,34]</sup> Therefore, introducing MWCNTs can improve cyclic performance, electrochemical stability, and can be used in a wide range of energy storage and electronics applications.<sup>[35–39]</sup>

In this study,  $\text{Sb}_2\text{Se}_3$  NRs were synthesized and combined with MWCNTs using a colloidal synthesis method. The properties of  $\text{Sb}_2\text{Se}_3$  NRs and  $\text{Sb}_2\text{Se}_3$  NRs@MWCNT were verified using various techniques, such as X-ray diffraction spectroscopy (XRD) and transmission electron microscopy (TEM). Electrochemical

[a] T. Jung,<sup>+</sup> Y. Jin,<sup>+</sup> J. Ha Moon, H. Seong, G. Kim, H. Yoo, S. Lee, Prof. S.-R. Kwon, Prof. S. Kuk Kim, Prof. J. Choi

Department of Chemistry, Institution: Gyeongsang National University, Jinju 52828, South Korea

E-mail: sungkukim@gnu.ac.kr  
cjw0910@gnu.ac.kr

[+] These authors contributed equally to this work.

 Supporting information for this article is available on the WWW under <https://doi.org/10.1002/batt.202400378>

tests were performed to evaluate the improved sodium-ion storage capability of  $\text{Sb}_2\text{Se}_3$  NRs@MWCNT without the need for additional conductive carbons.  $\text{Sb}_2\text{Se}_3$  NRs@MWCNT showed enhanced cycle performance (a capacity of  $440 \text{ mAhg}^{-1}$  at current density of  $0.1 \text{ Ag}^{-1}$ ) comparing to  $\text{Sb}_2\text{Se}_3$  NRs (a capacity of  $220 \text{ mAhg}^{-1}$  at current density of  $0.1 \text{ Ag}^{-1}$ ) in the voltage range between  $0.01$ – $2.8 \text{ V}$  ( $\text{V}$  vs  $\text{Na}/\text{Na}^+$ ). These findings indicate that  $\text{Sb}_2\text{Se}_3$  NRs@MWCNT exhibited superior cyclic performance and stability as an anode material for SIBs.

## Experimental Section

### Synthesis of $\text{Sb}_2\text{Se}_3$ NRs@MWCNT

First, the MWCNTs were functionalized in sulfuric acid/nitric acid (3:1, v/v) for 1 h with magnetic stirring at room temperature and sonicated for 8 h. Subsequently, the functionalized MWCNTs were harvested by filtration and rinsed with deionized water several times to a neutral pH and were dried at  $60^\circ\text{C}$  in a vacuum oven for 6 h. The pretreated MWCNTs were dispersed in 10 mL of oleylamine (Sigma-Aldrich), and the suspension was poured into a 50 mL Schlenk flask. The mixture was heated at  $120^\circ\text{C}$  for 1 h under vacuum conditions to dry the oleylamine surfactant. Then, 45 mg of Se powder (Acros Organics) and 65 mg of  $\text{SbCl}_3$  (Sigma-Aldrich) were added to the dried suspension and heated at  $205^\circ\text{C}$  for 20 min with magnetic stirring. After cooling to room temperature, the product was washed with methanol and hexane several times. The resulting product was centrifuged and dried at room temperature under vacuum conditions (Scheme S1).  $\text{Sb}_2\text{Se}_3$  NRs were synthesized using the same method except using pretreated MWCNTs to compare the electrochemical behavior with composite materials.

### Materials Characterization

The crystalline structure of  $\text{Sb}_2\text{Se}_3$  NRs and  $\text{Sb}_2\text{Se}_3$  NRs@MWCNT was analyzed by X-ray diffraction (XRD; MiniFlex 600, Rigaku, 40 kV and 15 mA,  $\text{Cu}-\text{K}\alpha$ , radiation) pattern, and the morphology of the samples was evaluated by scanning electron microscopy (SEM; JSM-7601F) with energy dispersive spectrometer (EDS; Ultim Max, Oxford Instruments), transmission electron microscopy (TEM; TF30ST, FEI). The Raman spectra of the samples was obtained using a Raman instrument (Renishaw Invia Raman Microscope) at a wavelength of 633 nm He–Ne Laser (50 W). X-ray photoelectron spectroscopy (XPS, Thermo VF scientific) data of these samples was measured with a mono chromatic photo energy of XPS ( $\text{Al K}\alpha$  1486.6 eV, 400  $\mu\text{m}$ , Scan 50, resolution 0.1 eV), respectively, and fitted by Lorentzian-Gaussian 80% and used linear background. The specific surface area can be evaluated by  $\text{N}_2$  adsorption-desorption isotherms that were measured using BELSORP-mini II (MicrotracBEL, Osaka, Japan).

### Electrochemical Measurements

The sodium-ion storage of the samples was tested with CR-2032 coin cells. A  $\text{Sb}_2\text{Se}_3$  NRs electrode was prepared as working electrode by mixing the  $\text{Sb}_2\text{Se}_3$  NRs powder with conductive carbon (Super P) and polyvinylidene fluoride (PVDF) at a weight ratio of 8:1:1 in a N-methyl-2-pyrrolidone (NMP) solvent. Another working electrode, a  $\text{Sb}_2\text{Se}_3$  NRs@MWCNT electrode, was prepared by mixing the  $\text{Sb}_2\text{Se}_3$  NRs@MWCNT powder and PVDF at a weight ratio of 9:1 in the NMP solvent. The resulting slurry was loaded onto Cu foil

and dried in a vacuum oven at  $80^\circ\text{C}$  for 3 h. Sodium metal was used as both the counter electrode and the reference electrode. Along with a glass fiber separator, and 1 M  $\text{NaPF}_6$  in a diethylene glycol dimethyl ether (DEGDME) was used as the electrolyte. The coin cells were assembled in an Ar-filled glovebox. Cyclic voltammetry test was performed using potentiostat ZIVE SP1 (from Wonatech) at a scan rate of  $2.0 \text{ mVs}^{-1}$ , and Galvanostatic charge-discharge performance was evaluated at room temperature using WBCS3000S (from Wonatech) in a voltage window of  $0.01$ – $2.8 \text{ V}$  (vs.  $\text{Na}/\text{Na}^+$ ).

## Results and Discussion

The morphologies of the  $\text{Sb}_2\text{Se}_3$  NRs and  $\text{Sb}_2\text{Se}_3$  NRs@ MWCNT were analyzed by SEM and TEM. The SEM images of  $\text{Sb}_2\text{Se}_3$  NRs and  $\text{Sb}_2\text{Se}_3$  NRs@MWCNT display rod-like structure with a diameter of approximately 80–90 nm and well mixed distribution of MWCNTs (Figure 1a and d). The nanorod  $\text{Sb}_2\text{Se}_3$  and MWCNTs were observed in the high-resolution TEM (HR-TEM) (Figure 1b and e), and the interplanar distance of 0.31 nm, corresponding to the (211) plane was well matched with XRD pattern (Figure 1c and f). The existence of Sb and Se elements for  $\text{Sb}_2\text{Se}_3$  NRs was demonstrated using EDS (Figure 1g–j). The Sb:Se ratio was close to 2:3, indicating that  $\text{Sb}_2\text{Se}_3$  NRs had been successfully fabricated.

All diffraction peaks of the  $\text{Sb}_2\text{Se}_3$  NRs and  $\text{Sb}_2\text{Se}_3$  NRs@ MWCNT in the XRD pattern were obtained from the orthorhombic crystal structure of  $\text{Sb}_2\text{Se}_3$  (JCPDS #15-0861) (Figure 2a). The peaks located at  $16.87^\circ$ ,  $27.39^\circ$ ,  $28.20^\circ$ ,  $31.15^\circ$ ,  $32.22^\circ$  and  $34.13^\circ$  can be assigned to (120), (230), (211), (221), (301) and (240) crystal planes, respectively.<sup>[40]</sup> It demonstrated high levels of crystallinity and purity with no inaccurate peaks of  $\text{Sb}_2\text{Se}_3$  NRs and  $\text{Sb}_2\text{Se}_3$  NRs@MWCNT. Raman spectroscopy

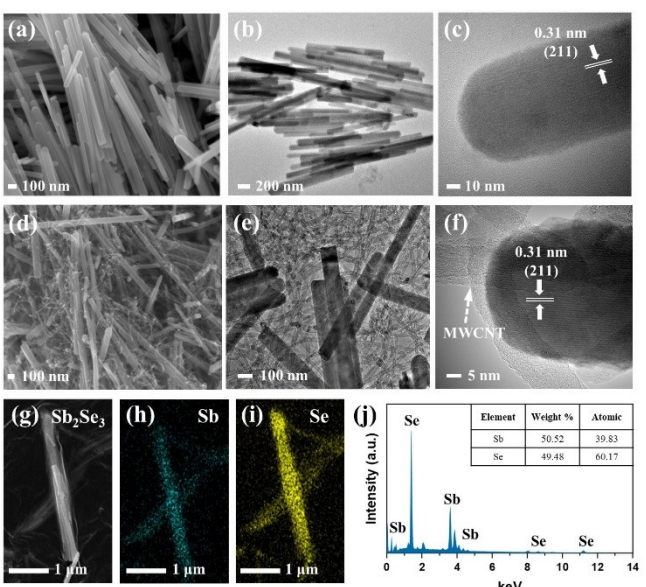


**Figure 1.** (a, g) SEM image, (b) TEM image, and (c) HR-TEM image of  $\text{Sb}_2\text{Se}_3$  NRs. (d) SEM image, (e) TEM image, and (f) HR-TEM image of  $\text{Sb}_2\text{Se}_3$  NRs@MWCNT. Elemental mapping image of (h) Antimony, (i) Selenium, (j) EDS spectrum.

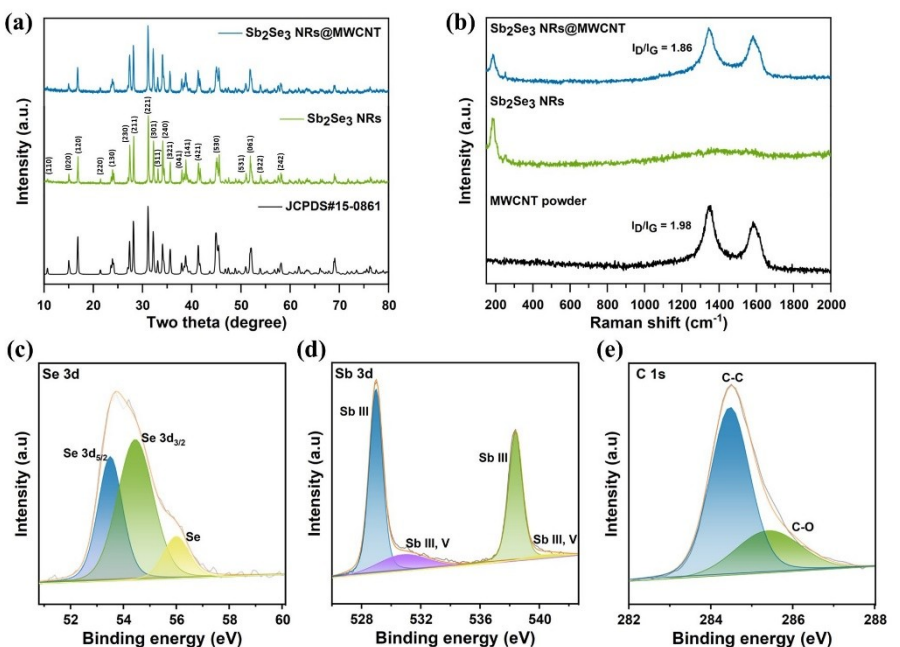
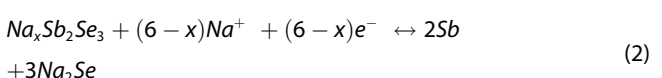


**Figure 2.** (a) XRD pattern of  $\text{Sb}_2\text{Se}_3$  NRs and  $\text{Sb}_2\text{Se}_3$  NRs@MWCNT. (b) Raman spectra of MWCNT powder,  $\text{Sb}_2\text{Se}_3$  NRs and  $\text{Sb}_2\text{Se}_3$  NRs@MWCNT. XPS spectra of (c) Se 3 d, (d) Sb 3 d, and (e) C 1s for  $\text{Sb}_2\text{Se}_3$  NRs@MWCNT.

was performed to confirm the presence of carbon in  $\text{Sb}_2\text{Se}_3$  NRs@MWCNT (Figure 2b). Two broad and high peaks were observed at  $1344$  and  $1583\text{ cm}^{-1}$ , corresponding to the D band and G band of carbons, indicating a disordered  $\text{sp}^2$  structure and a  $\text{sp}^2$  hybridized graphic structure, respectively. The  $I_{\text{D}}/I_{\text{G}}$  ratios were calculated as  $1.98$  for MWCNTs and  $1.86$  for  $\text{Sb}_2\text{Se}_3$  NRs@MWCNT. The decreased  $I_{\text{D}}/I_{\text{G}}$  ratio could indicate that the defective carbon structure reduced, and the graphitic structure increased, promoting the adsorption behavior of  $\text{Na}^+$ .<sup>[41,42]</sup> Additionally, the peaks at  $186$  and  $252\text{ cm}^{-1}$  each correspond to heteropolar Sb–Se vibrations and nonpolar Sb–Sb vibrations, respectively.<sup>[43]</sup> XPS was performed to confirm binding energy and composition (Figure 2c–e). Peaks for Sb 3 d ( $\sim 542.6\text{ eV}$ ), Se 3 d ( $\sim 60\text{ eV}$ ) and C 1s ( $\sim 288\text{ eV}$ ) were detected for  $\text{Sb}_2\text{Se}_3$  NRs@MWCNT, confirming the presence of Sb, Se, and C elements. The XPS peaks of Sb III and Sb III, V were observed at  $538.4$  and  $540.3\text{ eV}$  for Sb 3d<sub>3/2</sub>, respectively, while other peaks at  $529$  and  $530.9\text{ eV}$  were each assigned to Sb 3d<sub>5/2</sub>.<sup>[44]</sup> And the peaks at  $54.5$ ,  $53.5$ , and  $56.0\text{ eV}$  were assigned to Se 3d<sub>3/2</sub>, Se 3d<sub>5/2</sub>, and Se of  $\text{Se}^{2-}$ , respectively.<sup>[40,44]</sup> The C 1s peaks at  $284.6$  and  $285.4\text{ eV}$  corresponded to C–O and C–C.<sup>[45]</sup> The N<sub>2</sub> adsorption-desorption measurement was performed to confirm the specific surface area of  $\text{Sb}_2\text{Se}_3$  NRs and  $\text{Sb}_2\text{Se}_3$  NRs@MWCNT (Figure S1). The specific surface area of  $\text{Sb}_2\text{Se}_3$  NRs@MWCNT ( $41.57\text{ m}^2\text{ g}^{-1}$ ) was enhanced compared to  $\text{Sb}_2\text{Se}_3$  NRs ( $9.90\text{ m}^2\text{ g}^{-1}$ ) due to the introduction of MWCNTs.<sup>[15,27,32]</sup>

The CV test was performed on  $\text{Sb}_2\text{Se}_3$  NRs and  $\text{Sb}_2\text{Se}_3$  NRs@MWCNT at a scan rate of  $2\text{ mVs}^{-1}$  within a voltage range of  $0.01$ – $2.8\text{ V}$  to investigate their sodium storage properties (Figure 3a and b). The peak at  $1.80\text{ V}$  in the first cathodic scan of  $\text{Sb}_2\text{Se}_3$  NRs was attributed to the insertion of  $\text{Na}^+$  into the  $\text{Sb}_2\text{Se}_3$  host [Equation (1)], and the peak over  $0.70$ – $0.25\text{ V}$  was

ascribed to the conversion and alloying reaction process to form Sb,  $\text{Na}_2\text{Se}$ , and  $\text{Na}_x\text{Sb}$  [Equations (2 and 3)]. The peak at  $0.89\text{ V}$  was not observed in the subsequent cathodic sweep and it was associated with side reactions such as the formation of an irreversible solid electrolyte interphase (SEI) layer.<sup>[46,47]</sup> The peak at  $0.93\text{ V}$  in the anodic scan of  $\text{Sb}_2\text{Se}_3$  NRs was attributed to the dealloying reaction process to form Sb metal. And the peaks at  $1.54$  and  $1.88\text{ V}$  was ascribed to the reverse conversion reaction process between  $\text{Na}_2\text{Se}$  and Sb, and extraction of  $\text{Na}^+$ , respectively.<sup>[48]</sup> Compared with  $\text{Sb}_2\text{Se}_3$  NRs, CV curves for  $\text{Sb}_2\text{Se}_3$  NRs@MWCNT obviously showed reversible redox reaction. The cathodic peaks at  $1.64\text{ V}$ , and  $0.56$ ,  $0.40$ ,  $0.32$ ,  $0.26\text{ V}$  could be attributed to the insertion of  $\text{Na}^+$ , conversion, and alloying reaction processes. Additionally, the peak of the SEI layer, as previously mentioned, could be observed at  $0.93\text{ V}$ . The anodic peaks of  $0.80$ ,  $0.91\text{ V}$ , and  $1.61$ ,  $1.90\text{ V}$ , and  $2.44\text{ V}$  were ascribed to dealloying, the reverse conversion reaction process, and  $\text{Na}^+$  extraction, respectively.<sup>[32,46,48,49]</sup>



The charge-discharge (CD) curves of  $\text{Sb}_2\text{Se}_3$  NRs and  $\text{Sb}_2\text{Se}_3$  NRs@MWCNT were measured at a current density of  $0.1\text{ Ag}^{-1}$  in a voltage range of  $0.01$ – $2.8\text{ V}$  (Figure 3c and d). The initial charge/discharge capacities of  $\text{Sb}_2\text{Se}_3$  NRs and  $\text{Sb}_2\text{Se}_3$  NRs@MWCNT were  $338.9$ / $575.7\text{ mAhg}^{-1}$  and  $648.9$ / $826.4\text{ mAhg}^{-1}$ , with coulombic efficiencies (CE) of  $\approx 58.9\%$  and

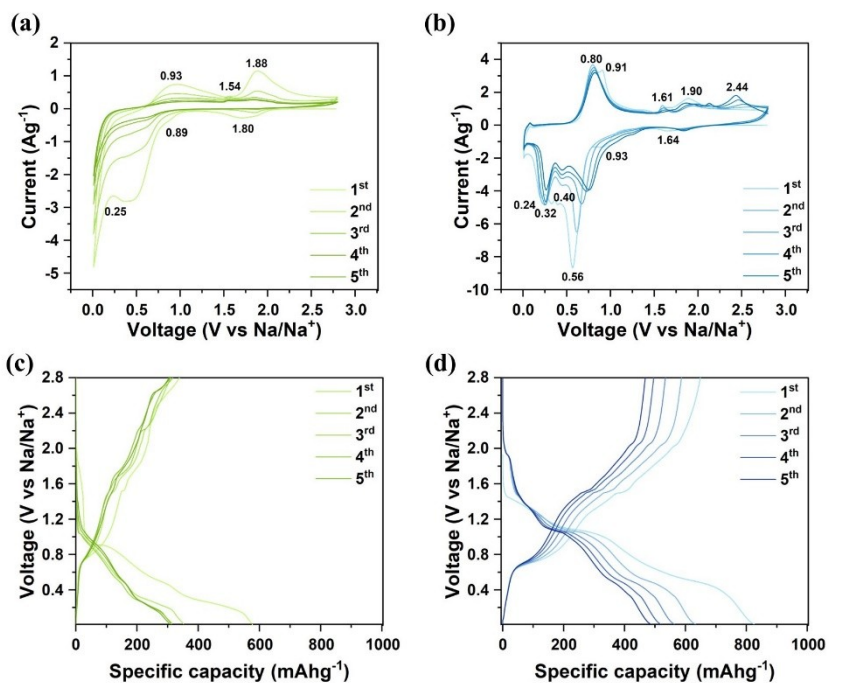


**Figure 3.** Cyclic voltammetry curves of (a)  $\text{Sb}_2\text{Se}_3$  NRs and (b)  $\text{Sb}_2\text{Se}_3$  NRs@MWCNT. Galvanostatic charge-discharge curves of (c)  $\text{Sb}_2\text{Se}_3$  NRs and (d)  $\text{Sb}_2\text{Se}_3$  NRs@MWCNT.

78.5%, respectively. In the following cycles, the charge/discharge capacities of  $\text{Sb}_2\text{Se}_3$  NRs and  $\text{Sb}_2\text{Se}_3$  NRs@MWCNT were  $310.1/357.8 \text{ mAh g}^{-1}$  and  $587.3/632.7 \text{ mAh g}^{-1}$ , each indicating higher CEs at  $\approx 88\%$  and  $92\%$ , respectively. The low CEs were attributed to the initial irreversible SEI layer and decomposition of the electrolyte.<sup>[32,49,50]</sup> In addition, when comparing the sodium diffusion coefficient value of  $\text{Sb}_2\text{Se}_3$  NRs to  $\text{Sb}_2\text{Se}_3$

NRs@MWCNT in the EIS test,  $\text{Sb}_2\text{Se}_3$  NRs@MWCNT showed good performance after the galvanostatic charge-discharge test (Figure S2). As a result, the highly conductive MWCNTs contributed to the improved electrochemical performance.

The rate performance of  $\text{Sb}_2\text{Se}_3$  NRs and  $\text{Sb}_2\text{Se}_3$  NRs@MWCNT was investigated at current densities at 0.1, 0.2, 0.5 and  $1.0 \text{ Ag}^{-1}$  over a voltage range of 0.01–2.8 V (Figure 4a). When

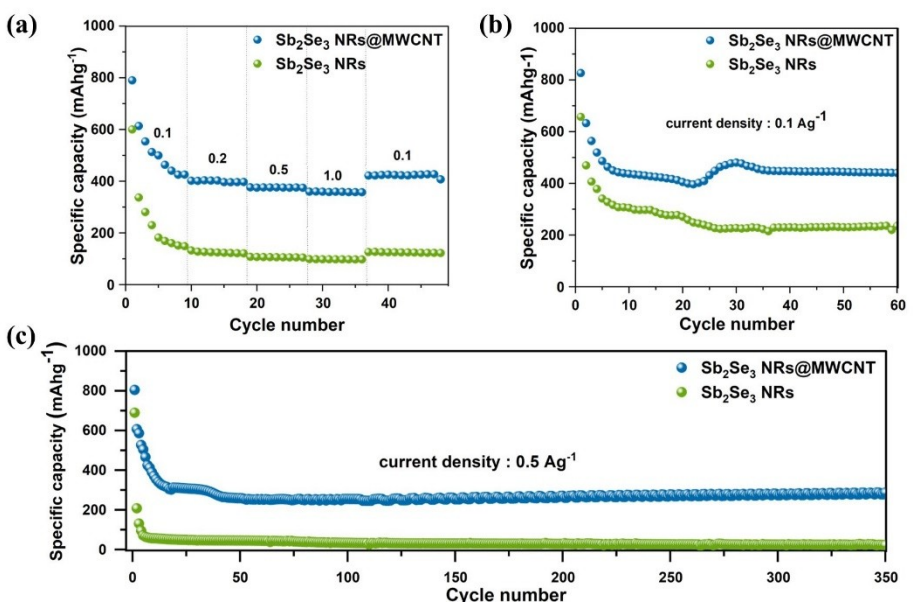


**Figure 4.** (a) Rate performance of  $\text{Sb}_2\text{Se}_3$  NRs and  $\text{Sb}_2\text{Se}_3$  NRs@MWCNT. Cycling performance of  $\text{Sb}_2\text{Se}_3$  NRs and  $\text{Sb}_2\text{Se}_3$  NRs@MWCNT at current density of (b)  $0.1 \text{ Ag}^{-1}$  and (c)  $0.5 \text{ Ag}^{-1}$ .

switching the current densities,  $\text{Sb}_2\text{Se}_3$  NRs@MWCNT showed almost similar capacity values, maintaining approximately  $360 \text{ mAhg}^{-1}$ . It was also confirmed that  $\text{Sb}_2\text{Se}_3$  NRs exhibited almost no difference in capacities under different current densities. though the values were lower. It indicated that  $\text{Sb}_2\text{Se}_3$  NRs and It indicated that  $\text{Sb}_2\text{Se}_3$  NRs and  $\text{Sb}_2\text{Se}_3$  NRs@MWCNT had good stability at various current densities, exhibiting little difference in performance between higher current densities and lower current densities. The cyclic performance of  $\text{Sb}_2\text{Se}_3$  NRs and  $\text{Sb}_2\text{Se}_3$  NRs@MWCNT was evaluated at current densities of  $0.1 \text{ Ag}^{-1}$  and  $0.5 \text{ Ag}^{-1}$  (Figure 4b and c). At a current density of  $0.1 \text{ Ag}^{-1}$ , the specific capacity of  $\text{Sb}_2\text{Se}_3$  NRs was  $235 \text{ mAhg}^{-1}$ , whereas the specific capacity of  $\text{Sb}_2\text{Se}_3$  NRs@MWCNT remained at  $440 \text{ mAhg}^{-1}$  after 60 cycles. At a higher current density of  $0.5 \text{ Ag}^{-1}$ , while the specific capacity of  $\text{Sb}_2\text{Se}_3$  NRs decreased dramatically, the specific capacity of  $\text{Sb}_2\text{Se}_3$  NRs@MWCNT remained to  $286 \text{ mAhg}^{-1}$  after 350 cycles. During the continuous cycling process of  $\text{Sb}_2\text{Se}_3$  NRs and  $\text{Sb}_2\text{Se}_3$  NRs@MWCNT, the capacity changes were caused by some side reactions.<sup>[14,51]</sup> Gradually, an unstable gel-like polymer film formed on the electrode surface, leading to capacity fading. This fragile film decomposed and repeatedly reconstructed, and stabilized during cycling.<sup>[28,52–54]</sup> Similar processes can be observed in other electrodes in LIBs and SIBs.<sup>[43,49,55–58]</sup> In addition, the morphology of the active material ( $\text{Sb}_2\text{Se}_3$  NRs and  $\text{Sb}_2\text{Se}_3$  NRs@MWCNT) was confirmed by comparing the SEM images of the electrodes that underwent constant current charge/discharge tests. The SEM images of cycled electrodes showed that rod-like  $\text{Sb}_2\text{Se}_3$  in  $\text{Sb}_2\text{Se}_3$  NRs@MWCNT electrode well maintained even after the sodiation/desodiation processes, while  $\text{Sb}_2\text{Se}_3$  in  $\text{Sb}_2\text{Se}_3$  NRs electrode decomposed (Figure S3). The presence of MWCNTs contributed to enhanced electrochemical performance and structural stability.

The in-situ electrochemical impedance spectroscopy (EIS) of  $\text{Sb}_2\text{Se}_3$  NRs@MWCNT was analyzed to investigate the mechanism and change in impedance at specific voltages during the charge and discharge process (Figure 5a–c). By measuring the EIS and galvanostatic charge-discharge test, we can observe the reaction at a specific voltage state through the Nyquist plot (discharge state: 1.7 V, 1.3 V, 0.65 V, 0.01 V, and charge state: 0.7 V, 1.35 V, 1.75 V, 2.8 V). To distinguish between the voltage values in a discharged state and charged state, “” is indicated in front of the voltage value in a discharged state. The Nyquist plot revealed a semicircle in high frequency and inclined lines in the low frequency region spanning from 1 MHz to 10 mHz, and the fitting process was performed using the recommended equivalent circuit (insert in Figure 5c).<sup>[59]</sup> At the 1.3 V discharge state, two semicircles and the decreased  $R_{ct}$  value were observed, which indicated the activation of the stable SEI layer. The  $R_{ct}$  value slightly increased because the conversion reaction induced phase change and volume expansion. During the charging process, the Nyquist plots reverted to showing a single semicircle. The  $R_{ct}$  value exhibited a minor increase but remained at a low value.<sup>[47,60]</sup> The galvanostatic intermittent titration technique (GITT) was employed to analyze the sodium diffusion coefficient of  $\text{Sb}_2\text{Se}_3$  NRs@MWCNT (Figure 5d–f). In the GITT measurement process, a short constant current was applied followed by a relaxation process. The electrode was discharged and charged at a current density of  $0.1 \text{ Ag}^{-1}$  for 6 minutes, followed by a relaxation period of 60 minutes. Diffusion coefficients of sodium ion ( $D_{\text{Na}}$ ) were calculated using the following Equation (4):<sup>[61]</sup>

$$D_{\text{Na}} = \frac{4}{\pi\tau} \left( \frac{m_B V_B}{M_B A} \right)^2 \left( \frac{\Delta E_S}{\Delta E_r} \right)^2 \left( \tau \ll \frac{L^2}{D_{\text{Na}}} \right) \quad (4)$$

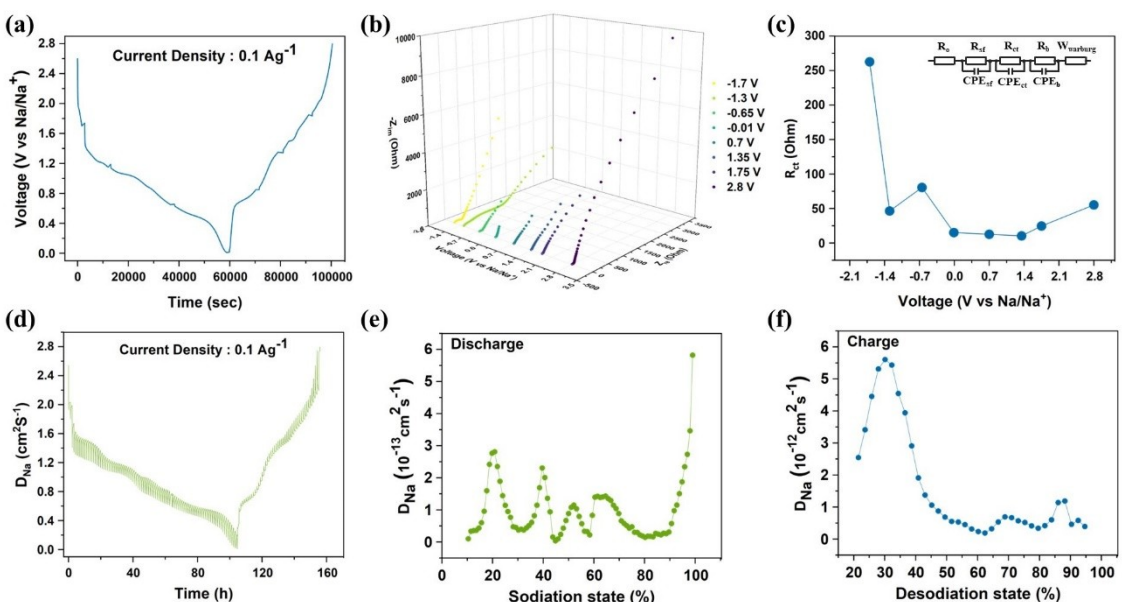


**Figure 5.** (a) Voltage and time curve at a current density of  $0.1 \text{ Ag}^{-1}$ , (b) In-situ Nyquist plots at several voltages and (c) Values of  $R_{ct}$  at specific voltages during the initial cycle of  $\text{Sb}_2\text{Se}_3$  NRs@MWCNT. (d) GITT curves of  $\text{Sb}_2\text{Se}_3$  NRs@MWCNT, and calculated diffusion coefficient for (e) Discharge and (f) Charge.

Where  $V_M$  is the molar volume ( $\text{cm}^3 \text{mol}^{-1}$ );  $M_B$  is the molar weight of the materials ( $\text{g mol}^{-1}$ );  $m_B$  is the mass of the active materials in an electrode (g); A is the electrode area ( $\text{cm}^2$ ); and  $\tau$  is the duration time.  $\Delta E_s$  and  $\Delta E_r$  were calculated from voltage differences during the duration and relaxation times (Figure S4). The GITT results were expressed as the function of  $D_{\text{Na}}$  vs sodiation (or desodiation) state during the discharge (or charge) process. The  $D_{\text{Na}}$  value exhibited an increase during the conversion and alloying reaction in the sodiation process (Figure 5e). This indicated that the reactions proceeded easily during the  $\text{Na}^+$  insertion. A similar tendency was also observed during the desodiation process, indicating effective  $\text{Na}^+$  extraction through dealloying and reverse conversion reaction (Figure 5f).

## Conclusions

In summary,  $\text{Sb}_2\text{Se}_3$  NRs were fabricated and combined with functionalized MWCNTs simply using a colloidal synthesis method. The XRD pattern and TEM images confirmed that deformation did not occur. The combined  $\text{Sb}_2\text{Se}_3$  NRs with MWCNTs exhibited an improved specific capacity (440  $\text{mAh g}^{-1}$  at 0.1  $\text{Ag}^{-1}$  after 60 cycles compared with 235  $\text{mAh g}^{-1}$  of pure  $\text{Sb}_2\text{Se}_3$  NRs) and cyclic stability (286  $\text{mAh g}^{-1}$  at 0.5  $\text{Ag}^{-1}$  after 350 cycles) as an anode for SIBs without additional conductive carbons like super P. The results indicated that the presence of MWCNTs could increase conductivity and alleviate the volume change associated with sodiation and desodiation, resulting in enhanced  $\text{Na}^+$  storage compared with pure  $\text{Sb}_2\text{Se}_3$  NRs. This work brings new insights of MWCNTs, which can provide stability for a conversion-alloying electrode, and  $\text{Sb}_2\text{Se}_3$  NRs@MWCNT as promising anode material of SIBs.

## Supporting Information Summary

The authors have cited additional references within the Supporting Information.

## Acknowledgements

T. Jung and Y. Jin contributed equally to this work. This work was supported by a National Research Foundation of Korea (NRF) grant funded by the Korean government (MSIT) (NRF-2021R1C1C1011436, 2022R1A4A1021817). This research was also supported by the "Regional Innovation Strategy (RIS)" through the NRF funded by the Ministry of Education (MOE) (2021RIS-003), and the following are results of a study on the "Leaders in Industry-university Cooperation3.0" Project, supported by the Ministry of Education and National Research Foundation of Korea. This work was supported by the Technological Development for Commercialization using a tech-bridge platform [RS-2022-00141871] funded by the Ministry of SMEs and Startups (MSS, Korea). This work was supported by the research grant of the Gyeongsang National University in

2023 and by Learning & Academic research institution for Master's-PhD students, and Postdocs (LAMP) Program of the National Research Foundation of Korea (NRF) grant funded by the Ministry of Education (RS-2023-00301974).

## Conflict of Interests

The authors declare no conflict of interest.

## Data Availability Statement

The data that support the findings of this study are available from the corresponding author upon reasonable request.

**Keywords:** Metal selenide • Antimony selenide • Multi-walled carbon nanotube • Sodium-ion battery • Anode

- [1] M. Armand, J.-M. Tarascon, *Building Better Batteries*, *Nature*. **2008**, *451*, 652–657.
- [2] J. C. Pramudita, D. Sehrawat, D. Goonetilleke, N. Sharma, *Adv. Energy Mater.* **2017**, *7*, 1602911.
- [3] S. U. D. Shamim, M. K. Hossain, S. M. Hasan, A. A. Piya, M. S. Rahman, M. A. Hossain, F. Ahmed, *Appl. Surf. Sci.* **2022**, *579*, 152147.
- [4] T. Liu, S. Hou, Q. Guo, Z. Liang, Z. Xiong, L. Zhao, *Appl. Surf. Sci.* **2022**, *579*, 152227.
- [5] Z. Zhang, Z. Gu, C. Zhang, J. Li, C. Wang, *Batter Supercaps* **2021**, *4*, 1680–1700.
- [6] Y. Kee, B. Put, N. Dimov, A. Staykov, S. Okada, *Batter Supercaps* **2020**, *3*, 402–408.
- [7] Q. Cu, C. Shang, L. Hu, G. Zhou, X. Wang, *Appl. Surf. Sci.* **2022**, *579*, 152181.
- [8] F. Li, Z. Zhou, *Small* **2018**, *14*, 1702961.
- [9] S. W. Kim, D. H. Seo, X. Ma, G. Ceder, K. Kang, *Adv. Energy Mater.* **2012**, *2*, 710–721.
- [10] M. D. Slater, D. Kim, E. Lee, C. S. Johnson, *Adv. Funct. Mater.* **2013**, *23*, 947–958.
- [11] F. Li, Y. Zhao, L. Xia, Z. Yang, J. Wei, Z. Zhou, *J. Mater. Chem. A Mater.* **2020**, *8*, 12391–12397.
- [12] M. Ma, K. Yao, Y. Wang, D. Fattakhova-Rohlfing, S. Chong, *Adv. Funct. Mater.* **2024**, *34*, 2315662.
- [13] Q. Zhou, H. K. Liu, S. X. Dou, S. Chong, *ACS Nano* **2024**, *18*, 7287–7297.
- [14] S. Qiao, Q. Zhou, M. Ma, H. K. Liu, S. X. Dou, S. Chong, *ACS Nano* **2023**, *17*, 11220–11252.
- [15] S. Chong, M. Ma, L. Yuan, S. Qiao, S. Dong, H. Liu, S. Dou, *Energy Enviro. Mater.* **2023**, *6*, 12458.
- [16] S. Komaba, W. Murata, T. Ishikawa, N. Yabuuchi, T. Ozeki, T. Nakayama, A. Ogata, K. Gotoh, K. Fujiwara, *Adv. Funct. Mater.* **2011**, *21*, 3859–3867.
- [17] Z. Zhu, F. Cheng, Z. Hu, Z. Niu, J. Chen, *J. Power Sources* **2015**, *293*, 626–634.
- [18] Y. Zhang, N. Wang, C. Sun, Z. Lu, P. Xue, B. Tang, Z. Bai, S. Dou, *Chem. Eng. J.* **2018**, *332*, 370–376.
- [19] Z. Lu, Y. Zhai, N. Wang, Y. Zhang, P. Xue, M. Guo, B. Tang, D. Huang, W. Wang, Z. Bai, S. Dou, *Chem. Eng. J.* **2020**, *380*, 122455.
- [20] X. Zhou, Y. Zhong, M. Yang, M. Hu, J. Wei, Z. Zhou, *Chem. Commun.* **2014**, *50*, 12888–12891.
- [21] Z. Hu, Q. Liu, S. L. Chou, S. X. Dou, *Adv. Mater.* **2017**, *29*, 1700606.
- [22] M. Ma, S. Chong, K. Yao, H. K. Liu, S. X. Dou, W. Huang, *Matter* **2023**, *6*, 3220–3273.
- [23] W. Li, M. Zhou, H. Li, K. Wang, S. Cheng, K. Jiang, *Electrochim. Commun.* **2015**, *60*, 74–77.
- [24] Y. Zhang, Q. Zhou, J. Zhu, Q. Yan, S. X. Dou, W. Sun, *Adv. Funct. Mater.* **2017**, *27*, 1702317.
- [25] H. Hou, M. Jing, Y. Yang, Y. Zhang, Y. Zhu, W. Song, X. Yang, X. Ji, *J. Mater. Chem. A Mater.* **2015**, *3*, 2971–2977.
- [26] S. Chong, T. Li, S. Qiao, Y. C. Yang, Z. Liu, J. Yang, H. Y. Tuan, G. Cao, W. Huang, *ACS Nano* **2024**, *18*, 3801–3813.

- [27] N. Wang, Z. Bai, Y. Qian, J. Yang, *Adv. Mater.* **2016**, *28*, 4126–4133.
- [28] Q. Li, W. Zhang, J. Peng, D. Yu, Z. Liang, W. Zhang, J. Wu, G. Wang, H. Li, S. Huang, *Adv. Funct. Mater.* **2022**, *32*, 2112776.
- [29] J. Li, D. Yan, X. Zhang, S. Hou, D. Li, T. Lu, Y. Yao, L. Pan, *Electrochim. Acta* **2017**, *228*, 436–446.
- [30] S. X. Wu, C. L. Chiang, C. C. Wang, C. Y. Chen, *J. Taiwan Inst. Chem. Eng.* **2018**, *89*, 208–214.
- [31] Y. Li, Y. Chen, W. Feng, F. Ding, X. Liu, *J. Power Sources* **2011**, *196*, 2246–2250.
- [32] M. Ihsan-Ul-Haq, H. Huang, J. Wu, N. Mubarak, A. Susca, Z. Luo, B. Huang, J. K. Kim, *Carbon N Y* **2021**, *171*, 119–129.
- [33] R. Chen, Y. Mao, Z. Li, F. Liu, F. Gao, *Mater. Chem. Phys.* **2023**, *293*, 126891.
- [34] J. K. Yoo, Y. Oh, T. Park, K. E. Lee, M. K. Um, J. W. Yi, *Energy Technol.* **2019**, *7*, 1800845.
- [35] C. Zhao, Z. Wang, X. Tan, H. Huang, Z. Song, Y. Sun, S. Cui, Q. Wei, W. Guo, R. Li, C. Yu, J. Qiu, X. Sun, *Small Methods* **2019**, *3*, 1800546.
- [36] M. Ihsan-Ul-Haq, H. Huang, J. Wu, J. Cui, S. Yao, W. G. Chong, B. Huang, J. K. Kim, *Nano Energy* **2020**, *71*, 104613.
- [37] G. Wang, H. Li, Q. Zhang, Z. Yu, M. Qu, J. *Solid State Electrochem.* **2011**, *15*, 759–764.
- [38] S. Jessl, D. Beesley, S. Engelke, C. J. Valentine, J. C. Stallard, N. Fleck, S. Ahmad, M. T. Cole, M. De Volder, *Mater. Sci. Eng. A* **2018**, *735*, 269–274.
- [39] Y. Cheng, H. Xie, L. Zhou, B. Shi, L. Guo, J. Huang, *Appl. Surf. Sci.* **2021**, *566*, 150645.
- [40] L. Guo, L. Cao, J. Huang, J. Li, S. Chen, *Sustain. Energy Fuels* **2020**, *4*, 797–808.
- [41] M. S. Dresselhaus, A. Jorio, M. Hofmann, G. Dresselhaus, R. Saito, *Nano Lett.* **2010**, *10*, 751–758.
- [42] A. C. Ferrari, J. Robertson, *Phys. Rev. B: Condens. Matter Mater. Phys.* **2001**, *64*, 075414.
- [43] J. Qian, Y. Chen, L. Wu, Y. Cao, X. Ai, H. Yang, *Chem. Commun.* **2012**, *48*, 7070–7072.
- [44] G. Xu, L. Ma, C. Gu, Z. Jie, X. Cui, C. Zhang, L. Liu, *Acta Mater.* **2022**, *240*, 118310.
- [45] J. Wang, B. Wang, X. Liu, J. Bai, H. Wang, G. Wang, *Chem. Eng. J.* **2020**, *382*, 123050.
- [46] X. Z. Li, S. H. Tian, Z. C. Lv, P. F. Wang, T. F. Yi, *Ceram. Int.* **2023**, *49*, 7414–7423.
- [47] P. Ge, X. Cao, H. Hou, S. Li, X. Ji, *ACS Appl. Mater. Interfaces* **2017**, *9* (40), 34979–34989.
- [48] Q. Li, P. Du, Y. Yuan, W. Yao, Z. Ma, B. Guo, Y. Lyu, P. Wang, H. Wang, A. Nie, R. Shahbazian-Yassar, J. Lu, *Nano Lett.* **2019**, *19* (5), 3074–3082.
- [49] X. Ou, C. Yang, X. Xiong, F. Zheng, Q. Pan, C. Jin, M. Liu, K. Huang, *Adv. Funct. Mater.* **2017**, *27*, 1606242.
- [50] W. Zhao, C. M. Li, *J. Colloid Interface Sci.* **2017**, *488*, 356–364.
- [51] S. K. Kim, H. K. You, K. R. Yun, J. H. Kim, T. Y. Seong, *Adv. Opt. Mater.* **2023**, *11* (7), 2202625.
- [52] Z. Lu, N. Wang, Y. Zhang, P. Xue, M. Guo, B. Tang, Z. Bai, S. Dou, *Electrochim. Acta* **2018**, *260*, 755–761.
- [53] X. Z. Li, Y. F. Guo, S. Zhao, P. F. Wang, Z. L. Liu, J. Shu, J. H. Zhang, T. F. Yi, *SIA* **2024**, *48*, 104275.
- [54] J. Zhu, Z. Yin, D. Yang, T. Sun, H. Yu, H. E. Hostler, H. H. Hng, H. Zhang, Q. Yan, *Energy Environ. Sci.* **2013**, *6*, 987–993.
- [55] M. Wan, R. Zeng, K. Chen, G. Liu, W. Chen, L. Wang, N. Zhang, L. Xue, W. Zhang, Y. Huang, *Energy Storage Mater.* **2018**, *10*, 114–121.
- [56] L. Hu, J. Pan, P. Zhao, G. Shi, B. Wang, F. Huang, *Mater. Adv.* **2022**, *3*, 3554–3561.
- [57] X. Xu, Y. Liu, X. Luo, G. Ma, F. Tian, Y. Li, D. Zhang, J. Yang, *Energy Storage Mater.* **2021**, *40*, 189–196.
- [58] S. Liu, D. Li, G. Zhang, D. Sun, J. Zhou, H. Song, *ACS Appl. Mater. Interfaces* **2018**, *10*, 34193–34201.
- [59] S. H. Lim, G. D. Park, D. S. Jung, J. H. Lee, Y. C. Kang, *J. Mater. Chem. A Mater.* **2020**, *8*, 1939–1946.
- [60] S. S. Zhang, K. Xu, T. R. Jow, *Electrochim. Acta* **2006**, *51*, 1636–1640.
- [61] Q. Pang, W. He, X. Yu, S. Yang, H. Zhao, Y. Fu, M. Xing, Y. Tian, X. Luo, Y. Wei, *Appl. Surf. Sci.* **2021**, *538*, 148043.

Manuscript received: June 12, 2024

Revised manuscript received: July 15, 2024

Accepted manuscript online: August 1, 2024

Version of record online: October 15, 2024